processes

MDPI

Article

One-Pot Synthesis of $Ni_{0.05}Ce_{0.95}O_{2-\delta}$ Catalysts with Nanocubes and Nanorods Morphology for CO_2 Methanation Reaction and in Operando DRIFT Analysis of Intermediate Species

Igor Luisetto [1,*], Stefano Stendardo [1,*], Sakkarapalayam Murugesan Senthil Kumar [2], Karuppiah Selvakumar [2], Jagadesh Kopula Kesavan [3], Giovanna Iucci [3], Umberto Pasqual Laverdura [3] and Simonetta Tuti [3]

1 Italian National Agency for New Technologies, Energy and Sustainable Economic Development (ENEA), Via Anguillarese 301, 00123 Rome, Italy
2 Materials Electrochemistry Division, CSIR—Central Electrochemical Research Institute, Karaikudi 630003, India; senthilkumarsm@cecri.res.in (S.M.S.K.); selvakumarkaruppiah@cecri.res.in (K.S.)
3 Department of Science, Roma Tre University, Via della Vasca Navale 79, 00146 Rome, Italy; jagadesh.kopulakesvan@uniroma3.it (J.K.K.); giovanna.iucci@uniroma3.it (G.I.); umberto.pasquallaverdura@uniroma3.it (U.P.L.); simonetta.tuti@uniroma3.it (S.T.)
* Correspondence: igor.luisetto@enea.it (I.L.); stefano.stendardo@enea.it (S.S.)

Citation: Luisetto, I.; Stendardo, S.; Senthil Kumar, S.M.; Selvakumar, K.; Kesavan, J.K.; Iucci, G.; Pasqual Laverdura, U.; Tuti, S. One-Pot Synthesis of $Ni_{0.05}Ce_{0.95}O_{2-\delta}$ Catalysts with Nanocubes and Nanorods Morphology for CO_2 Methanation Reaction and in Operando DRIFT Analysis of Intermediate Species. *Processes* **2021**, *9*, 1899. https://doi.org/10.3390/pr9111899

Academic Editor: Jose Maria Corrêa Bueno

Received: 9 September 2021
Accepted: 21 October 2021
Published: 25 October 2021

Abstract: The valorization of CO_2 via renewable energy sources allows one to obtain carbon-neutral fuels through its hydrogenation, like methane. In this study, $Ni_{0.05}Ce_{0.95}O_{2-\delta}$ catalysts were prepared using a simple one-pot hydrothermal method yielding nanorod and nanocube particles to be used for the methanation reaction. Samples were characterized by XRD, BET, TEM, H_2-TPR, and H_2-TPD experiments. The catalytic activity tests revealed that the best performing catalyst was $Ni_{0.05}Ce_{0.95}O_{2-\delta}$, with nanorod morphology, which gave a CO_2 conversion of 40% with a selectivity of CH_4 as high as 93%, operating at 325 °C and a GHSV of 240,000 $cm^3\ h^{-1}\ g^{-1}$. However, the lower activation energy was found for $Ni_{0.05}Ce_{0.95}O_{2-\delta}$ catalysts with nanocube morphology. Furthermore, an in operando diffuse reflectance infrared Fourier transform spectroscopy (DRIFTS) analysis was performed flowing CO_2:H_2 or CO:H_2 mixture, showing that the main reaction pathway, for the CO_2 methanation, is the direct hydrogenation of formate intermediate.

Keywords: CO_2 methanation; in operando DRIFT; reaction mechanism; CeO_2 morphology; nickel catalyst

1. Introduction

A reduction of carbon emissions from industry and energy production by avoiding, capturing, or recycling carbon is urgently needed to limit the ever-increasing concentration of CO_2 in the atmosphere, the leading cause of global warming. The utilization of CO_2 as a C1 building block in organic synthesis to produce chemicals is limited to the production of urea, salicylic acid, and polycarbonates, and utilizes only a small percentage of the largely available feedstock [1]. Recycling CO_2 to produce fuels such as methane, methanol, dimethyl ether, or higher alcohols could be a convenient alternative that has not been thoroughly investigated yet. Research in this field may leads to reduced consumption of carbon-based fossil fuels, avoiding the introduction of new CO_2 to the atmosphere [2,3]. The hydrogenation of CO_2 to produce methane and water, ($CO_2 + 4H_2 \rightarrow CH_4 + 2H_2O$), known as Sabatier reaction or methanation, is exothermic (ΔH° = –164 kJ mol^{-1}), and thermodynamically favored (ΔG^0 = –131 kJ/mol), but with kinetic barriers that require the presence of a catalyst. CO_2 methanation is currently attracting much attention due to its potential application in the power to gas process (PtG), where the intermittent excess electricity, generated from renewable sources, can be used for the sustainable production

of synthetic natural gas (SNG), which contributes to the reduction of greenhouse gas emissions by replacing natural fossil methane [4,5].

In the presence of a catalyst, CO_2 methanation occurs above 200 °C, and is generally exploited below 400 °C, to limit the endothermic side reactions that occur at high temperatures: the reverse-water-gas shift (RWGS: $CO_2 + H_2 \rightarrow CO + H_2O$, $\Delta H^\circ = 41$ kJ mol^{-1}), which produces CO instead of methane, and the reforming of methane with CO_2 ($CH_4 + CO_2 \rightarrow 2CO + 2H_2$, $\Delta H^\circ = 247$ kJ mol^{-1}). Noble and transition metals of the VIII-X groups (Ru, Rh, Ir, Pd, Ni, Fe, Co), are active and selective for methanation. They have been supported on oxides (γ-Al_2O_3, TiO_2, SiO_2, ZrO_2, CeO_2), and extensively studied, as summarized in some recent reviews [2,4,6–11]. The order of the metal elements for the specific activity or selectivity may differ in published papers, depending on the methanation conditions and on the metal/support interactions; anyhow, ruthenium is generally the most active. Nonetheless, Ni metal is the most commonly used for commercial applications, due to its high activity, high selectivity, and very low cost. However, Ni-based catalysts are more active at higher temperatures than noble metal, and are prone to deactivation by carbon deposition due to the Boudouard reaction and the reduction by H_2 of CO_2 and CO to carbon. The catalytic performances of Ni-based catalysts depend markedly on the properties of the support, which affect the dispersion of the catalytic phase, the reducibility of the metal, and the metal-support interactions.

The mechanism of CO_2 methanation over nickel-based catalysts has been extensively studied using theoretical and experimental approaches, but many aspects of the mechanism remain controversial, and are still debated among researchers. Three main possible reaction mechanisms have been proposed [11–13]: the first pathway involves the associative adsorption of CO_2 with a surface H*, forming a formate intermediate (CHOO*), which is subsequently hydrogenated to CH*, and then to CH_4 (formate pathway). The other mechanisms both start with the dissociative adsorption of CO_2 onto CO* and O*, followed by the hydrogenation of CO_{ad} to form methane after direct cleavage of the C-O bond, or via an HCO* intermediate. However, in the last two routes, the intermediate is the adsorbed CO. The properties of the support and the operating conditions appear to influence the preferred reaction pathway and the rate-determining step. The methanation mechanisms on Ni supported on CeO_2 catalysts are still under investigation and can be deepened by analyzing the involved intermediates, using in operando DRIFT experiments [12,14]

CeO_2 is one of the most studied catalyst carriers, due to its redox properties, and to its ability to store and release oxygen (oxygen storage capacity, OSC) through the Ce^{3+}/Ce^{4+} couple on the surface, and due to its oxygen vacancies. CeO_2-based catalysts showed excellent performances in the oxidation of CO [15] or alcohols [16], combustion of methane in the lean state [17], dry reforming [18–20], hydrogenation [21], and CO_2 methanation [14,22]. The redox properties and the ability to highly disperse Ni have been suggested as responsible for the excellent catalytic activity and stability for CO_2 methanation [23,24].

CeO_2 can be prepared in different nano-shapes, such as nano-rod, nano-cubic or nano-octahedra. The morphology affects the catalytic performances of Me/CeO_2 catalysts for various reactions: i.e., CO_2 methanation over Ni [3,25], methane combustion over Pd [17], water gas shift reaction over Cu [26], dry reforming of methane or methanol over Ni [27,28], hydrogenation of ethyl levulinate over Ru [21]. The nano-rod morphology appears the most active and stable for all these reactions, whereas the order of activity for nano-cubes and nano-octahedra may be reversed.

The difference in activity of Me/CeO_2 catalysts with different nano-shapes is ascribed to differences in the specific exposed crystallographic facets that affect the metal/support interactions [3,27,29], the amount of oxygen vacancies [3,17,21,25,27–29], or acid-basic sites [28]. Experimental and theoretical studies on well-defined nanocrystals have established that the control of exposed facets in ceria is a promising way to direct the activity and selectivity of many reactions [29].

In light of these considerations and perspectives, it is interesting to further investigate the role of most active nanoshapes for the CO_2 methanation, i.e., rods and cubes.

Recently, we studied a series of Ni/nanorod-CeO_2 catalysts with different Ni loading (2–13 wt%) [22] and a Pd (2 wt%)/nanorod-CeO_2 [16], prepared by one-pot hydrothermal synthesis, founding that this preparation method allows one to obtain the high and homogeneous dispersion of supported metals, good stability of metal dispersion and support morphology after treatments at high temperatures.

In this work, we investigated the influence of morphology on catalytic activity for the CO_2 methanation of samples $Ce_{0.95}Ni_{0.05}O_{2-d}$, with nanorod or nanocube shape prepared by one-pot hydrothermal synthesis. This rapid and straightforward method ensures a high dispersion of nickel and a strong Ni-support interaction. The central core of this research is the study of the nature of reaction intermediates, and the dependence of their nature on the specific ceria nano-shape, through in operando DRIFT analysis.

2. Materials and Methods

2.1. Catalysts Synthesis

$Ce_{0.95}Ni_{0.05}O_{1.95}$ nanorods (Ni-nR): 2.97 g of $Ce(NO_3)_3 \times 6H_2O$ and 0.10 g of $Ni(NO_3)_2 \times 6H_2O$ were dissolved in 20 mL of distilled water. A NaOH solution (48 g of NaOH in 100 mL of distilled water) was added dropwise, with vigorous stirring for 30 min. After precipitation, the suspension was transferred to a Teflon-lined cylinder and kept in a hot oven for 24 h at 100 °C. The precipitate was washed to neutral pH, dried overnight at 80 °C, and ground in an agate mortar; the powder thus obtained was calcined at 500 °C for 5 h. CeO_2 nanorods (nR) were synthesized in the same way without a Ni reagent.

$Ce_{0.95}Ni_{0.05}O_{1.95}$ nanocubes (Ni-nC): 3.56 g of $Ce(NO_3)_3 \times 6H_2O$ and 0.13 g of $Ni(NO_3)_2 \times 6H_2O$ were dissolved in 20 mL of distilled water. A NaOH solution (29 g of NaOH in 100 mL of distilled water) was added dropwise with vigorous stirring for 30 min. After precipitation, the suspension was transferred to a Teflon-lined cylinder and kept in a hot oven for 24 h at 180 °C. The precipitate was washed to neutral pH, dried overnight at 80 °C, and ground in an agate mortar; the powder thus obtained was calcined at 500 °C for 5 h. CeO_2 nanocubes (nC) were synthesized in the same way without Ni reagent.

The chemical composition was checked using the EDAX technique integrated with the device TEM. The nominal composition was guaranteed with an error of ±5% regarding the different areas studied, confirming the nominal nickel content and, therefore, the accuracy of the hydrothermal synthesis method.

2.2. Catalysts Characterization

Powder X-ray diffraction patterns were recorded using a Scintag X1 diffractometer equipped, with a Cu Kα (λ = 1.5418 Å) source and the Brag-Brentano θ–θ configuration in the 2θ range 20–80°, with 0.05 step size and 3 s acquisition time. The NiO crystallite sizes were estimated by Scherrer Equation (1), where: D is the crystallite size in nm, K is the crystallite-shape factor, λ is the X-ray wavelength, β_D is the full-width at half maximum in radians, and ϑ is the Bragg angle.

$$D = \frac{K\lambda}{\beta_D cos\ \theta} \quad (1)$$

The lattice constant (α) of CeO_2 was calculated by the following Equation (2):

$$\alpha = \frac{\lambda}{2sin\ \theta}\sqrt{h^2 + k^2 + l^2} \quad (2)$$

The supports and catalysts XRD patterns were further elaborated by the Williamson plot to obtain the effects of size and strain in the CeO_2 crystals. The full width at half maximum β_T of the diffraction peak is ascribed to the broadening effect of both the

crystallite size β_D and the lattice strain β_s, arising from strain-induced broadening ε, according to the following Equations (3) and (4)

$$\beta_T = \beta_D + \beta_S = \frac{K\lambda}{Dcos\,\theta} + 4\varepsilon\,tan\,\theta \quad (3)$$

$$\beta_T cos\,\theta = \frac{K\lambda}{D} + 4\varepsilon\,sin\,\theta \quad (4)$$

The N_2 adsorption-desorption isotherms of the samples were obtained at −196.1 °C using a Micromeritics Gemini V apparatus. Prior to measurement, the samples were heated at 300 °C for 4 h in He. The specific surface area (SSA) was calculated by the Brunauer–Emmet–Teller (BET) method in the equilibrium pressure range of $0.05 < p/p^\circ < 0.3$. The pore size distribution was obtained from the branch of the desorption isotherm using the Barrett–Halenda (BJH) method. The total pore volume was calculated from the maximum adsorption point at $p/p^\circ = 0.98$.

Temperature-programmed reduction (TPR) and temperature-programmed desorption (TPD) of H_2 were performed using a Thermo Scientific TPDRO1100 flow-through apparatus. Before the experiments, the calcined sample was placed into a quartz reactor, and pre-treated flowing 20 $cm^3\ min^{-1}$ of 5% O_2/He gas mixture at 500 °C for 1 h, and cooled down to 50 °C. TPR was conducted by flowing 30 $cm^3\ min^{-1}$ of 5% H_2/Ar gas mixture, raising the temperature up to 1000 °C, with a heating rate of 10 °C min^{-1}. For TPD experiment, the calcined sample was pre-reduced flowing 30 $cm^3\ min^{-1}$ of 5% H_2/Ar gas mixture up to 500 °C for 1 h, then cooled down to 50 °C. The H_2 physisorbed was removed flowing 30 $cm^3\ min^{-1}$ of Ar for 1 h, then the temperature was increased up to 500 °C, with a heating rate of 10 °C min^{-1}. The H_2 consumption/chemisorption was measured by a TCD detector, calibrated by reducing a known amount of CuO (99.99% purity from Sigma Aldrich). A trap removed the H_2O generated in the reduction before flowing into the TCD detector. The Ni dispersion (D%) and the particle size of Ni (d) were calculated by Equations (5) and (6), respectively:

$$D(\%) = \frac{\eta SM}{W} \times 10^2 \quad (5)$$

$$d(\mathrm{nm}) = \frac{fW}{\rho\eta N_A SA} \times 10^5 \quad (6)$$

in these equations, f is the geometric shape factor (6 for spherical particles), W is the weight percentage of Ni (1.75%), ρ is the density of Ni (8.9 g/cm^3); η is the desorbed H_2 (mol/g), N_A is the Avogadro number (6.023×10^{23}), S is the stoichiometric factor for H_2 chemisorption (metal mole/gas mole = 2), A is the area occupied by the Ni surface atom (6.51×10^{-16} cm^2), M is the atomic mass of Ni (58.69 g/mol).

For the calculations of the theoretical hydrogen consumption to be compared with the experimental, the oxidation state of Ni = +2 and that of Ce = +4, was assumed. From the reaction: $20Ni_{0.05}Ce_{0.95}O_{1.95} + 10.5H_{2(g)} = Ni^0 + 9.5Ce_2O_3 + 10.5H_2O_{(g)}$, per gram of catalyst, the mmol of H_2 consumed for Ni is 0.30 mmol H_2/g, while that required for the reduction of CeO_2 to Ce_2O_3 is 2.84 mmol H_2/g.

A Tecnai G2 F20 s-twin instrument operating at 200 kV performed transmission electron microscopy (TEM) analysis.

Diffuse reflectance infrared Fourier transform spectroscopy (DRIFT) analysis was carried out using a Thermo-electron Corporation Nicolet 4700-FTIR spectrometer coupled to a reaction cell. The reactor unit was embedded with two $6 \times 90^\circ$ off-axis ellipsoidal mirrors arranged to discriminate specularly reflected radiation. Spectra were acquired with 256 scans in the flow of gases controlled by mass flow controllers. The sample was reduced in situ by flowing 50 $cm^3\ min^{-1}$ of 50% H_2/He gas mixture, heating up to 500 °C at a rate of 10 °C min^{-1}, and maintaining this temperature for 30 min. The DRIFT spectra of the reduced samples were acquired as background in the 100-500 °C temperature range at intervals of 100 °C. The methanation reaction mixture CO_2:H_2:He = 5:20:25 $cm^3\ min^{-1}$

or CO:H_2:He = 5:15:30 cm^3 min^{-1} flowed on the sample, and the spectra were recorded in the same temperature range of the backgrounds.

2.3. Fixed-Bed Catalytic Test

The CO_2 methanation reaction was performed in a fixed-bed quartz reactor, with an internal diameter of 6 mm and a length of 300 mm, inserted into a cylindrical oven. The reactive mixture was fed by three independent mass flow controllers with a CO_2:H_2:N_2 ratio of 1:4:5 and a total flow of 100 cm^3 min^{-1}, and a weight hourly space velocity (WHSV) of 60,000 $cm^3 g^{-1} h^{-1}$. Before the catalytic test, the sample was reduced in situ with a 50% H_2/N_2 stream (50 cm^3 min^{-1}), raising the temperature from RT to 500 °C, and held isothermally at this temperature for 60 min. The catalytic test was performed in the temperature range from 500 °C to 250 °C, with 25 °C decrements. A cold trap and a dryer removed H_2O from the flow before the analysis. The dry gas was analyzed by Agilent 7820 gas chromatograph. The conversion of CO_2 (X_{CO_2}) the selectivity of CH_4 (S_{CH_4}) and the yields of CH_4 (Y_{CH_4}) and CO (Y_{CO}) were calculated by Equations (7)–(9), where $CO_{2,\,out}$, $CH_{4,\,out}$ and CO_{out} are the gas volume concentrations in the effluent:

$$X_{CO_2}(\%) = \frac{CH_{4,\,out} + CO_{out}}{CO_{2,\,out} + CH_{4,\,out} + CO_{out}} \times 10^2 \quad (7)$$

$$S_{CH_4}(\%) = \frac{CH_{4,\,out}}{CH_{4,\,out} + CO_{out}} \times 10^2 \quad (8)$$

$$Y_{CH_4}\ or\ Y_{CO}(\%) = \frac{CH_{4,\,out}\ or\ CO_{out}}{CO_{2,\,out} + CH_{4,\,out} + CO_{out}} \times 10^2 \quad (9)$$

The turn over frequency TOF (s^{-1}) was calculated using Equation (10), where: $F_{CO_{2,\,in}}$ is the CO_2 flux in the reactor, $X_{CO_2}(\%)$ is the CO_2 conversion, M_{Ni} is the Ni molar mass, m_{cat} is the catalyst mass, $W_{Ni}(\%)$ is the Ni weight percentage, $D(\%)$ is the Ni dispersion obtained by the H_2-TPD technique.

$$TOF_{CO_2}\left(s^{-1}\right) = \frac{F_{CO_{2,\,in}}\ X_{CO_2}(\%) M_{Ni}}{m_{cat} W_{Ni}(\%) D(\%)} = \frac{-r_{CO_2} M_{Ni}}{W_{Ni}(\%) D(\%)} \quad (10)$$

3. Results

3.1. Structural and Morphological Characterization

The XRD patterns of the nR and nC supports and the Ni-nR and Ni-nC catalysts are shown in Figure 1A, and the corresponding Williamson–Hall (W-H) plots are given in Figure 1B. The main structural features are listed in Table 1. After calcination at 550 °C, the nR and nC supports showed the peaks corresponding to the diffraction planes (111), (200), (220), (311), (400), and (331) of the cubic structure with Fm3-3m space group (JCPDS 34-0394). The diffraction angle of these peaks was similar for both samples. However, the FWHM was much larger in the nR support, indicating a smaller crystallites size. In fact, from the intercept with the y-axis of the W-H plot, a crystallite size of 10 nm was calculated for the nR, compared to a much larger size, of 40 nm, obtained for the nC. The ε strain, resulting from the slope of the line, was also slightly different, being 1.7×10^{-3} and 1.4×10^{-3} for the nR and nC supports, respectively. Confirming a larger crystalline imperfection for the nanorod morphology, even if these defects did not change the lattice parameter, which was equal to 5.41 Å in both supports.

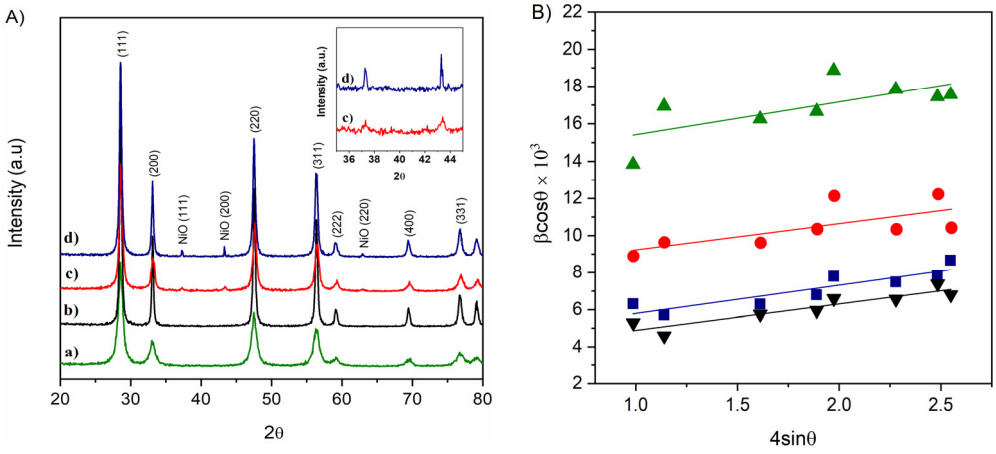

Figure 1. (**A**) X-ray diffraction patterns of: (a) nR; (b) nC; (c) Ni-nR; (d) Ni-nC. Patterns in the range 2θ = 45–45° showing the NiO peaks. (**B**) Williamson–Hall plots of: (▲) nR; (▼) nC; (●) Ni-nR; (■) Ni-nC.

Table 1. Structural parameters of as prepared samples.

Sample	$D_{W\text{-}H}$ (nm) [a]	ε	a (Å)	D_{NiO} (nm) [b]
nC	40	1.4×10^{-3}	5.41	
Ni-nC	32	1.5×10^{-3}	5.41	71
nR	10	1.7×10^{-3}	5.41	
Ni-nR	18	1.4×10^{-3}	5.40	20

[a] Calculated by the Williamson–Hall plot method. [b] Calculated by the Scherrer equation.

Introducing Ni during the synthesis significantly changed the crystallographic patterns of the catalysts calcined at 550 °C. Peaks at 2θ angles 37.3°, 43.3°, and 62.9° corresponding to diffraction planes (111), (200), and (220) of the cubic NiO phase with space group Fm3-3m (JCPDS 47-1049) were clearly visible, albeit with very low intensity due to the small amount of Ni in the catalysts (1.75 wt%). The width of these peaks was much larger in Ni-nR than in Ni-nC, and the crystallite sizes, estimated by the Scherrer equation, were 20 and 71 nm, respectively. From W–H diagrams of CeO_2 phase, crystallites of 18 nm and 32 nm with the strain of 1.4×10^{-3} and 1.5×10^{-3} were obtained for the Ni-nR and Ni-nC catalysts, respectively. The Ni-nR lattice parameter of 5.40 Å was slightly lower than that of Ni-nC, which was 5.41 Å. Thus, the introduction of Ni seems to reduce the crystallographic differences between the two morphologies. However, as reported by several authors [30,31], it cannot be ruled out that some of the Ni has been incorporated into the CeO_2 lattice to form a solid Ce-O-Ni solution.

The N_2 adsorption/desorption isotherms and the corresponding pore size distributions of the materials are shown in Figure 2, and the main textural properties are summarized in Table 2. All samples showed II-type adsorption–desorption curves, with H2-type hysteresis loop (IUPAC classification [32]), characteristic of macroporous materials. The specific surface area (SSA) of pure ceria was 32 m^2g^{-1} for nC morphology, and 92 m^2g^{-1} for nR morphology, agreeing with the different crystallite dimensions measured by XRD analysis. The addition of nickel led to a decrease in SSA of about 30% (62 m^2g^{-1}) only for the nR morphology, whereas it did not affect the surface area for the nanocube morphology. Bare nC and nR supports showed a Barrett–Joyner–Halenda (BJH) total pore volume equal to 0.24 and 0.36 $cm^3\ g^{-1}$, respectively. The addition of nickel caused an identical slight pore volume decrease of 8.3% in both samples (Table 2). The pore size distributions (PSD) for both structures showed a bimodal distribution with two maxima; one in the mesopores region (<10 nm), and another in the meso-macropores region (>50 nm). For the nC morphology, the maximum of the mesopores was centered at 2.5 nm, and that of the meso-macropores maximum at around 40 nm. The addition of nickel did not affect the overall distribution, probably due to a lower interaction between the metal and the

support. Quite the opposite was true for the nR morphology, where the introduction of nickel drastically changed the pore size distribution. In the as-is support, the mesopores maximum was at 3.5 nm. A much broader distribution of meso-macropores, between 10 nm and 70 nm, was detected, whereas, in the Ni-nR sample, the PSD of the small mesopores moved at a slightly smaller size of about 2.5 nm but, significantly, a narrower distribution of mesopores with a center around 14 nm was detected; additionally, few pores with sizes larger than 30 nm were found.

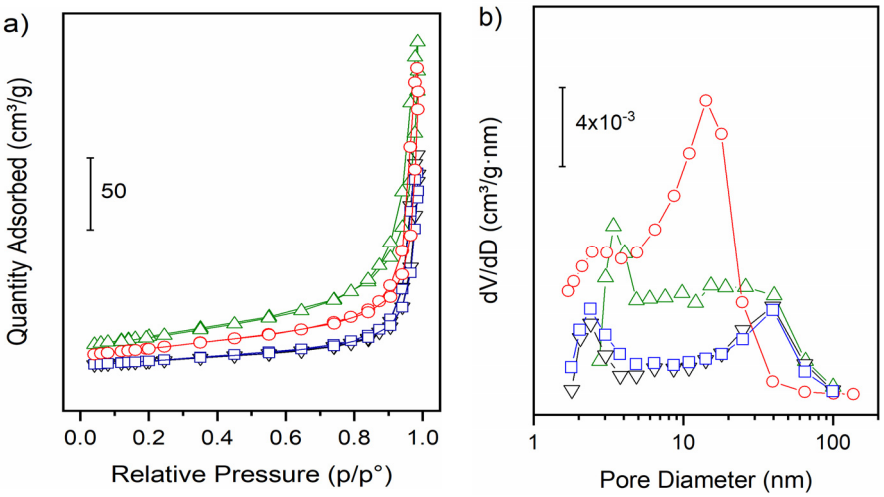

Figure 2. N_2 physisorption isotherms (**a**) and pore size distribution (**b**) of: (▲) nR; (▼) nC; (●) Ni-nR; (■) Ni-nC.

Table 2. Textural properties of as-prepared samples.

Sample	SSA (m^2g^{-1})	Pore Volume (cm^3g^{-1})	Average Pore Diameter (nm)
nC	32	2.4×10^{-1}	25
Ni-nC	33	2.2×10^{-1}	21
nR	92	3.6×10^{-1}	19
Ni-nR	62	3.3×10^{-1}	20

3.2. Temperature-Programmed Reduction (TPR) and Desorption (TPD) Characterization

The reducibility of the supports and associated Ni catalysts at increasing temperature (TPR) is shown in Figure 3A and the measured hydrogen consumption is listed in Table 3. The nC and nR carriers had two reduction regions labeled β and γ, respectively. The β region of the nC support (Figure 3A(a)) was characterized by two overlapping peaks, with the maximum at temperatures of 495 and 538 °C. For the nR support (Figure 3A(c)), the reduction occurred at lower temperatures and showed a much more intense peak, with the maximum at 507 °C, and a weak shoulder at 400 °C. Besides, a slightly negative signal was highlighted at about 620 °C due to the concomitant reduction of carbonates that were not removed with the pretreatment. The measured hydrogen consumption was proportional to the specific surface area, i.e., nR > nC. According to the literature, these peaks are attributable to the reduction in the first layers of the ceria surface [33]. It also depends on the exposed crystallographic planes [34], which are different for cubic and nanorod morphology. In the γ region, reduction began with a remarkably similar trend for both supports; a single large peak with the maximum at about 900 °C was evident, which did not go up to the highest temperature of 1000 °C. This peak was due to the reduction in the bulk of ceria, which was similar for both supports, not depending on the exposed surface. The intensity was lower in the nR than in the nC, due to a more significant proportion of ceria being reduced at lower temperatures [35].

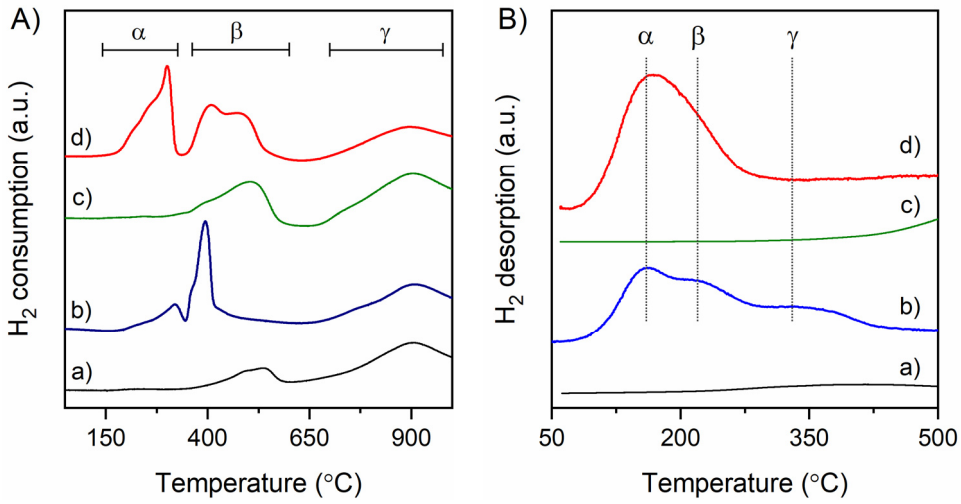

Figure 3. (**A**) TPR and (**B**) TPD profiles of: (**a**) nC, (**b**) Ni-nC, (**c**) nR, (**d**) Ni-nR.

Table 3. Amount of hydrogen consumed during TPR measurements. Ni dispersion, *D* (%), and the active Ni sites dimension, *d* (nm), determined from TPD analyzes..

Sample	Hydrogen Consumption/mmol g^{-1}				*D* (%)	*d* (nm)
	α	β	γ	Total		
nC		0.16	1.05	1.20		
Ni-nC	0.12	0.32	1.03	1.47	14	7
nR		0.38	0.79	1.17		
Ni-nR	0.44	0.53	0.67	1.64	20	5

The TPR profiles of the Ni-catalysts depended on the morphology of the CeO_2 support. The reduction of Ni^{2+} occurred in two temperature ranges, between 130–340 °C, called the α region, and between 350–450 °C, i.e., superimposed on the reduction temperature of the bare CeO_2 surface in the β region. The α region of the Ni-nC catalyst (Figure 3A(b)) consisted of two weak overlapping peaks at 280 °C, while the Ni-nR one (Figure 3A(d)) showed three more intense and overlapping peaks with a maximum at 270 °C. According to the literature, the α peaks corresponded to the reduction of O_2^{2-} chemisorbed on the vacancies formed by some Ni^{2+} ions in solid solution with CeO_2 [36]. However, a high hydrogen consumption was evident in the Ni-nR sample (0.44 mmol·g^{-1}), which was more significant than the reduction of Ni loading itself (0.30 mmol·g^{-1}), suggesting a remarkable reduction of the CeO_2 surface, as previously reported in the literature [37]. Peaks in the β region were assigned to the simultaneous reduction of NiO and the CeO_2 surface, the latter in a temperature range not different from that observed in the bare support. The hydrogen consumption of the Ni-nC sample (0.44 mmol·g^{-1}) in the α and β regions was very similar to what would be expected from the reduction of NiO and the CeO_2 surface of the bare support, indicating a lower interaction of NiO, with CeO_2 having a nanocube morphology. Instead, in the case of Ni-nR the consumption was significantly higher (0.97 mmol·g^{-1}), confirming a strong interaction of NiO with the CeO_2 surface with nanorod morphology, favouring the $Ce^{4+} \rightarrow Ce^{3+}$ reduction. Indeed, the percentage of Ce^{3+} of the Ni-nR catalyst was about 23%, much higher than that of the nR support, which was about 13%, while, for the Ni-nC catalyst and the nC support, the percentage of Ce^{3+} was essentially the same, about 5%. On the other hand, the reduction of ceria bulk was not significantly affected by the introduction of Ni, and it occurred in the same temperature range (γ region).

The temperature-programmed desorption trend of chemisorbed hydrogen (TPD) with respect to the supports and the Ni catalysts are shown in Figure 3. From this analysis, the dispersion D (%) and the particle size d (nm) of the active Ni sites was determined, and reported in Table 3. The TPD profile of the nC support showed a very weak peak at

about 400 °C, while the nR one revealed a more intense peak that started at temperatures higher than 400 °C without ending until 500 °C. These labile peaks were due to the release of chemisorbed H_2 from the CeO_2 surface. The TPD of the Ni-nC catalyst showed three peaks at about 160, 220, and 330 °C, which were due to the desorption of H_2 from the Ni^0 surface with different H-binding strength. From the peak area, the *D* (%) was 14%, and the dimension of the catalytically active Ni sites was *d* (nm) = 7. The Ni-nR catalyst exhibited a different TPD profile, with a single large peak, which was much more intense with a maximum at about 165 °C, indicating a more homogeneous H-binding strength over the Ni active surface; the *D* (%) was 20%, and the size of the active sites was *d* (nm) = 5.

3.3. TEM Characterization of the Synthesized Catalysts

TEM images of the synthesized catalysts are shown in Figure 4, and the size distributions are shown in Figure S1. Ni-nR showed the characteristic morphology of the nanorods, with mean CeO_2 width and length values of 14 ± 4 and 169 ± 68 nm, respectively. Some NiO particles with spherical morphology and an average size of 7 ± 4 nm were observed. Ni-nC showed CeO_2 particles with nanocube morphology, with quite heterogeneous dimensions of 27 ± 12 nm. Moreover, significantly smaller NiO particles were seen with an average dimension of 10 ± 3 nm, larger than those observed for Ni-nR. The NiO particle size distribution was in agreement with the crystallite size determined by XRD analysis using the Scherrer equation.

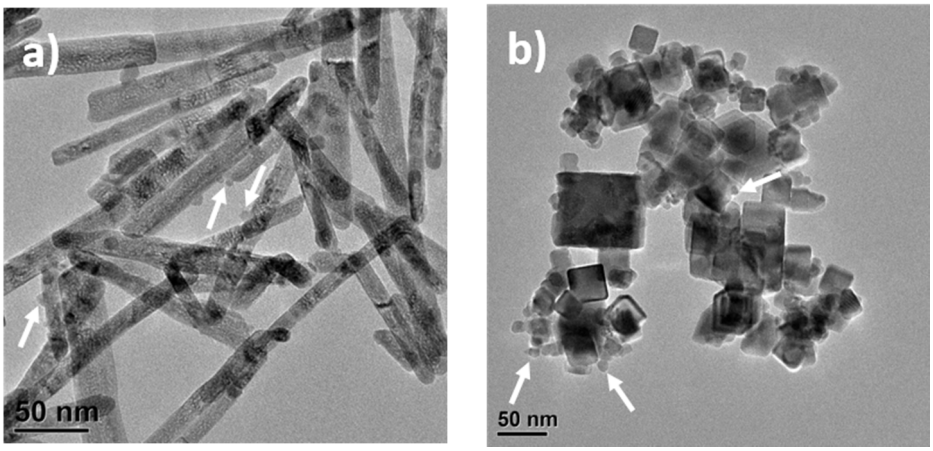

Figure 4. TEM images of Ni-nR (**a**) and Ni-nC (**b**) catalysts calcined at 550 °C. The arrows in the figure (**a**,**b**) points to the NiO particles.

These results are consistent with the reports of several authors. The morphology of CeO_2 varies from nanorods to nanocubes, as the temperature increases in the hydrothermal process [38]. For NiO, a strong effect of the temperature used in the hydrothermal process on the morphology and particles size was also demonstrated. In general, an increase in the nanoparticles size was obtained at higher temperatures [39,40].

3.4. Catalytic Activity

The catalytic activity performances were evaluated in the temperature range of 200–500 °C, as shown in Figure 5a. Although CO_2 methanation is strongly exothermic and thermodynamically favored at low temperatures, the conversion threshold for both catalysts began above 275 °C. The CO_2 conversion light-off curve of the Ni-nR catalyst increased rapidly to a maximum of about 55% at 400 °C, and then remained constant until 500 °C. The Ni-nC catalyst showed a much lower conversion. For example, at 325 °C, the conversion was 12%, while it reached a value of 40% for the Ni-nR catalyst. However, due to the progressively increasing trend, a conversion of about 48% was obtained at 500 °C, which is not different from that obtained with the nanorod morphology. It is essential to mention that the CeO_2 supports did not exhibit any catalytic activity under the assumed

conditions. Only the nanorod form conversion of about 2%, mainly to CO, was observed at the highest temperature of 500 °C.

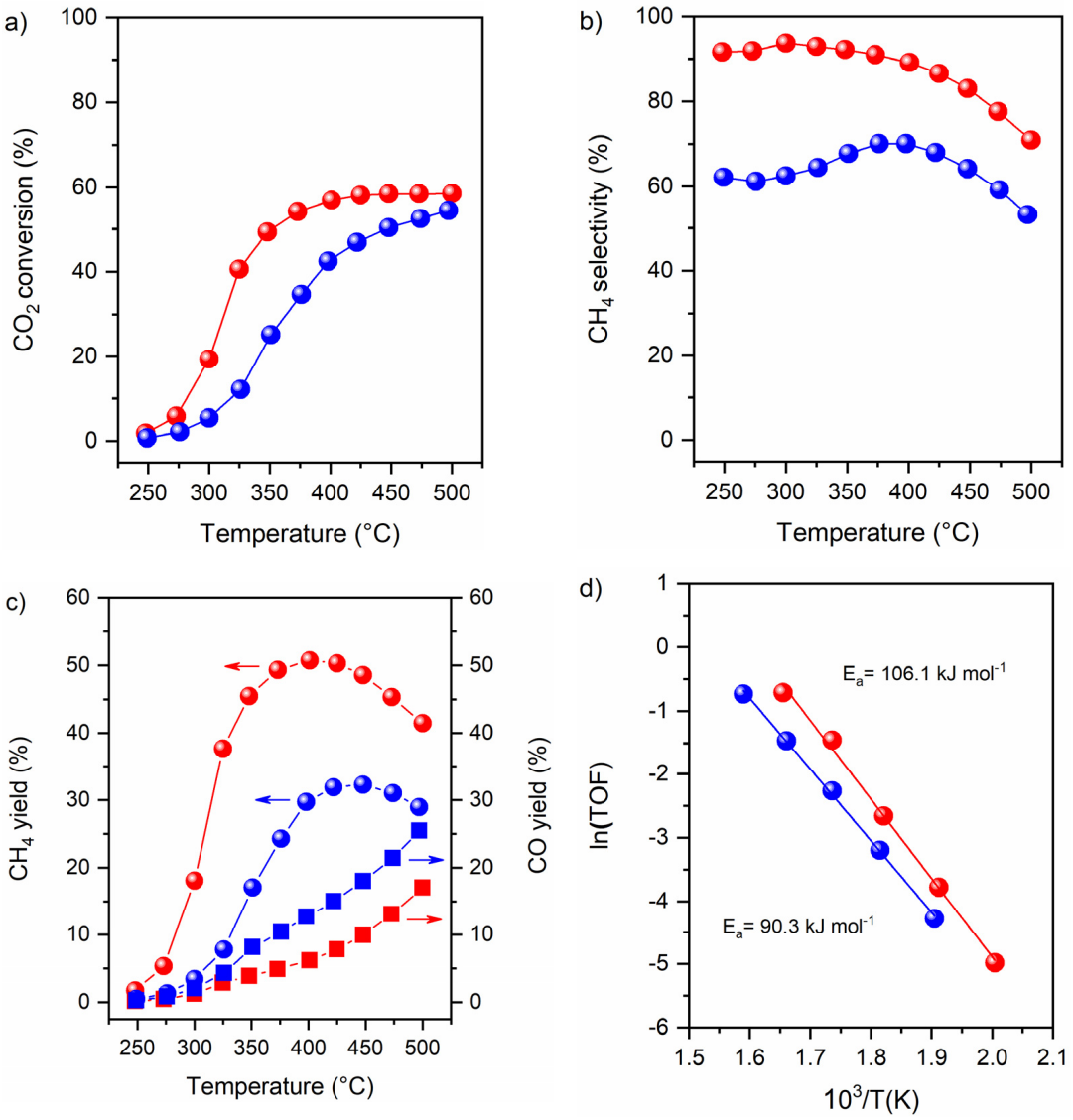

Figure 5. The catalytic activity of Ni-nR (symbols in red color) and Ni-nC (symbols in blue color) catalysts: (**a**) CO_2 conversion; (**b**) CH_4 selectivity; (**c**) CH_4 (circle symbols) and CO yields (square symbols); (**d**) Arrhenius plot of CO_2 conversion TOFs.

The selectivity to methane is plotted in Figure 5b. It was significantly higher for the Ni-nR, starting from 90% at 250 °C, and gradually decreasing to 70% at the highest temperature of 500 °C, while a particular trend was observed for the Ni-nC, where the selectivity started from 62% at 250 °C, and reached a maximum of 70% at 370 °C, and then decreased again to 53% at 500 °C. The yields of methane and carbon monoxide are reported in Figure 5c. The CH_4 yield had an increasing trend, reaching a maximum of 51% at 400 °C for the Ni-nR and 32% at 450 °C for the Ni-nC, and decreased again at higher temperatures. On the other hand, the yield of CO increased exponentially for both catalysts, but it was significantly lower for the Ni-nR, reaching 17% at 500 °C in contrast to a value of 25% observed for the Ni-nC one.

From the Arrhenius plot of TOF for CO_2 reduction rate shown in Figure 5d, the apparent activation energies were 90.3 and 106.1 kJ mol^{-1} for the Ni-nC and Ni-nR catalysts, respectively. The slight difference in the activation energy can be attributed to the exposed

crystallographic plane of ceria, involved in CO_2 activation, and the Ni particle size's effect on the interaction with H_2 and CO_2. In particular, the surface of CeO_2, with the nanocube morphology, exposes only the (100) faces, while the nanorod morphology exposes both the (110) and (100) faces [34,41]. The effect of such exposed faces on the formation of oxygen vacancies is not fully defined [42]. The role of Ni particle sizes on the reaction mechanism, affecting the selectivity to CH_4, may also significantly alter the apparent activation energy [43]. Moreover, the TOF increased for smaller metal size, e.g., the TOF of the Ni-nR sample with a Ni^0 particle size of 5 nm was 0.23 s^{-1} at 300 °C, while the TOF of the Ni-nC sample with a Ni^0 size of 7 nm decreased significantly to 0.10 s^{-1}. This confirms a positive effect of the nanorod morphology on the catalytic activity, also due to the larger dispersion of the active Ni sites.

To further highlight the differences among the Ni-nR and Ni-nC, the kinetic rate expressed by a power-low model $-r_{CO_2} = k \cdot P_{H_2}^x \cdot P_{CO_2}^y$ was determined at 350 °C at different reactant partial pressures with a WHSV of 240,000 $cm^3 g^{-1} h^{-1}$, ensuring reactant conversions of less than 15%. The logarithmic dependence of the kinetic rate on the partial pressure of the reactants is shown in Figure 6. Although the different reactive steps involved in the kinetics were not highlighted, this was an essential method to compare the two catalysts. The Ni-nR catalyst showed a clear dependence of the CO_2 conversion rate on the increase of the H_2 partial pressure, resulting in an apparent reaction order of $x_{H_2} = 0.68$, while the effect of the CO_2 partial pressure was negligible and the apparent reaction order was $y_{CO_2} = 0.06$. Therefore, the rate equation could be approximated as a near first-order dependence on H_2 pressure: $-r_{CO_2} = k \cdot P_{H_2}^{0.68} \cdot P_{CO_2}^{0.06} \approx k \cdot P_{H_2}^{0.68}$. For the Ni-nC catalyst, the influence of the H_2 partial pressure on the CO_2 conversion rate was much less pronounced with a value $x_{H_2} = 0.22$, and the contribution of CO_2 pressure was even smaller, showing an apparent reaction order $y_{CO_2} = 0.10$, which was only slightly higher than that observed for the Ni-nR catalyst. For Ni-nC, the following rate equation was expressed: $-r_{CO_2} = k \cdot P_{H_2}^{0.22} \cdot P_{CO_2}^{0.10}$. The negligible dependence of the reaction rate on the partial pressure of CO_2 suggests that CO_2 is primarily activated by the exposed surface of the CeO_2 supports, having proper surface basicity [38]. Indeed, in previous work [44], a negative dependence of the CO_2 conversion rate on Ni/YSZ catalyst was observed, indicating that both reactants should be activated on the Ni catalytically active surface.

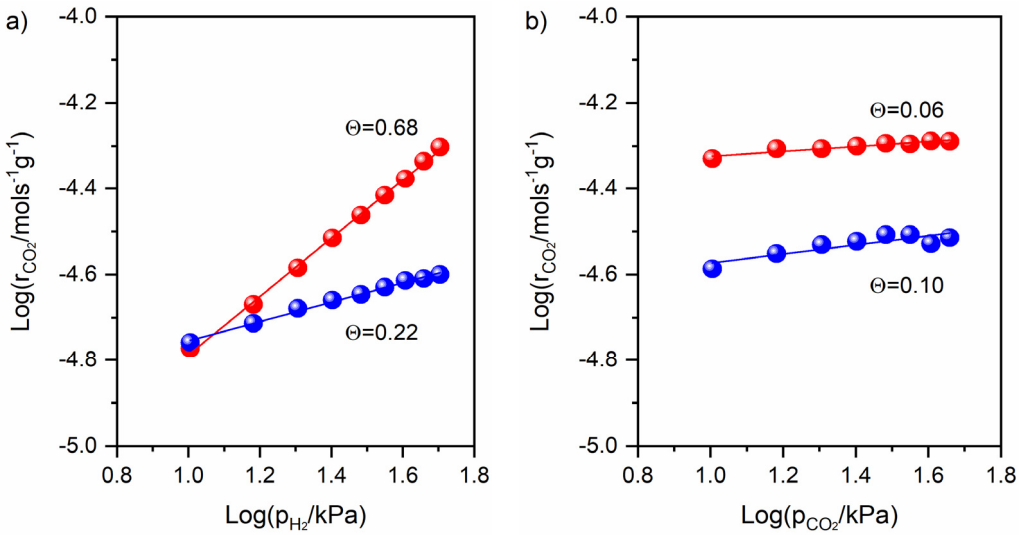

Figure 6. Effect of reactant partial pressure on CO_2 conversion rate for Ni-nR (symbols in red color) and Ni-nC (symbols in blue color): (**a**) H_2 partial pressure in the 10.1–50.7 kPa range at constant CO_2 partial pressure of 10.1 kPa; (**b**) CO_2 partial pressure in the 10.1–45.6 kPa range at constant H_2 partial pressure of 40.6 kPa.

After the catalytic test, which had a total duration of 10 h, the best performing Ni-nR catalyst was characterized by HR-TEM, as shown in Figure 7. The CeO_2 particles remained

with a rod-like morphology without sintering or morphological changes, and the average dimensions were 13 ± 3 nm for the diameter and 236 ± 43 nm for the length (Figure 7a). The Ni^0 showed particles with sizes of 8.6 ± 1.5 nm, thus in good agreement with the dimensions of the catalytically active Ni sites (5 nm) determined by the TPD of H_2. Higher magnification (Figure 7b) revealed that the actual distance between CeO_2 (111) planes was 3.5 Å, consistent with the value of calcined catalysts. The STEM analysis (Figure 7c) showed that the Ni particles were evenly distributed, although some aggregation could be seen in some parts, indicating their partial sintering. Carbon deposits were not observed, since, feeding an H_2/CO_2 ratio of 4, they were thermodynamically unfavorable [45].

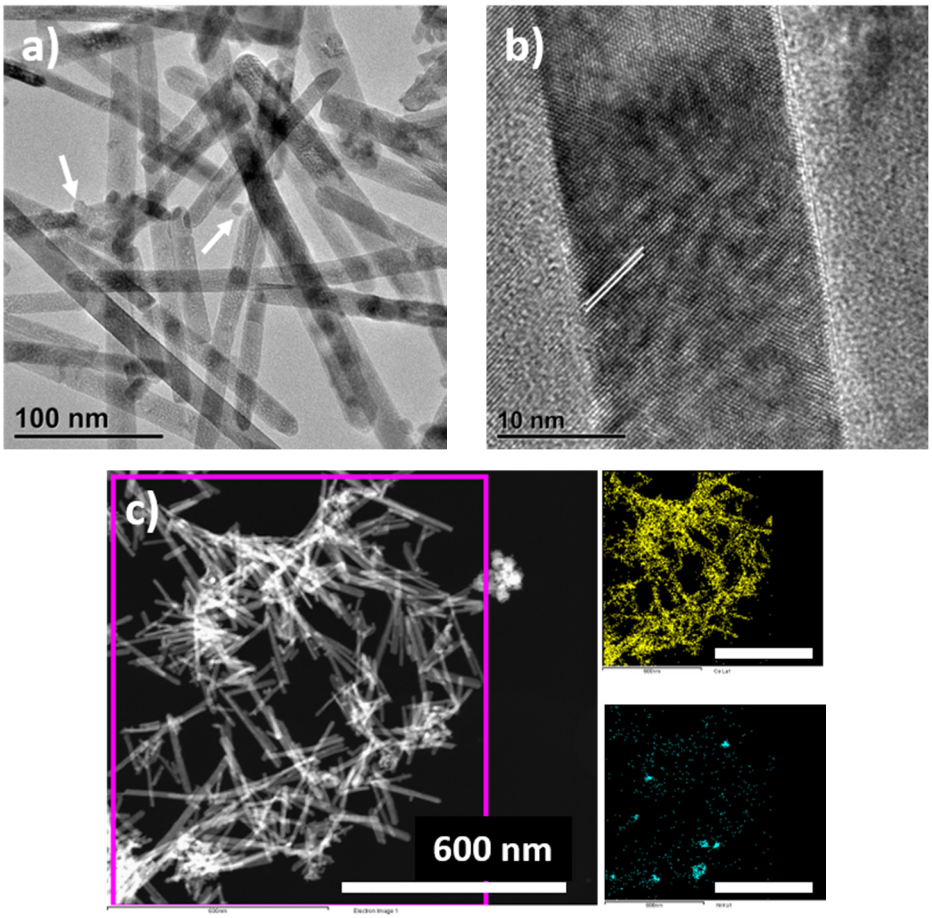

Figure 7. HR-TEM micrograph of Ni-nR catalyst after catalytic test at low (**a**) and high magnification (**b**), STEM imaging with Ce-L, and Ni-k mapping (**c**). The arrow in panel (**a**) points to the Ni particles.

3.5. DRIFT

To elucidate the reaction pathway, the nR and the Ni-nR samples were analyzed using the DRIFT technique. The significant species detected on the surface are listed in Table 4. The DRIFT spectra of nR are seen in the range between 4000 and 2600 cm^{-1} (Figure 8a) and between 2100 and 1150 cm^{-1} (Figure 8b). Two bands around 3710 and 3618 cm^{-1} were identified in the hydroxide vibrational region due to mono-coordinated -OH (type I) and bridged -OH (type II) vibrations on $Ce^{\delta+}$ site [46–49]. These bands occurred at all temperatures but were most intense at 300 °C. At this distinct temperature, a further signal at 3507 cm^{-1} was also uncovered, which could be due to vibrations of triple-bridged -OH on $Ce^{\delta+}$ site or to the hydroxyl group of bicarbonate species [50,51]. As the temperature increased, the intensity of this band gradually decreased and, at 500 °C, it was difficult to detect.

Table 4. Assignments and wavenumbers (cm^{-1}) of the prominent DRIFT bands formed during the CO_2 and CO methanation.

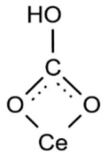 *Bidentate bicarbonate*	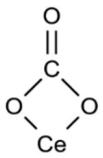 *Bidentate carbonate*	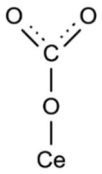 *Monodentate carbonate*	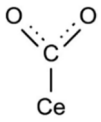 *Carboxylate*	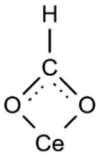 *Bidentate formate*	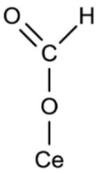 *Monodentate formate*
1612 $\nu_a(CO_3)$ 1390 $\nu_s(CO_3)$ 1216 δ(OH)	1562 $\nu_a(CO_3)$ 1272 $\nu_s(CO_3)$	1462 $\nu_a(CO_3)$ 1293 $\nu_s(CO_3)$	1465 $\nu_a(CO_2)$	2931 $\nu_a(CO_2)$ + δ(CH) 2845 ν(CH) 1569 $\nu_a(CO_2)$ 1352 $\nu_s(CO_2)$ + δ(CH)	1602 $\nu_a(CO_2)$

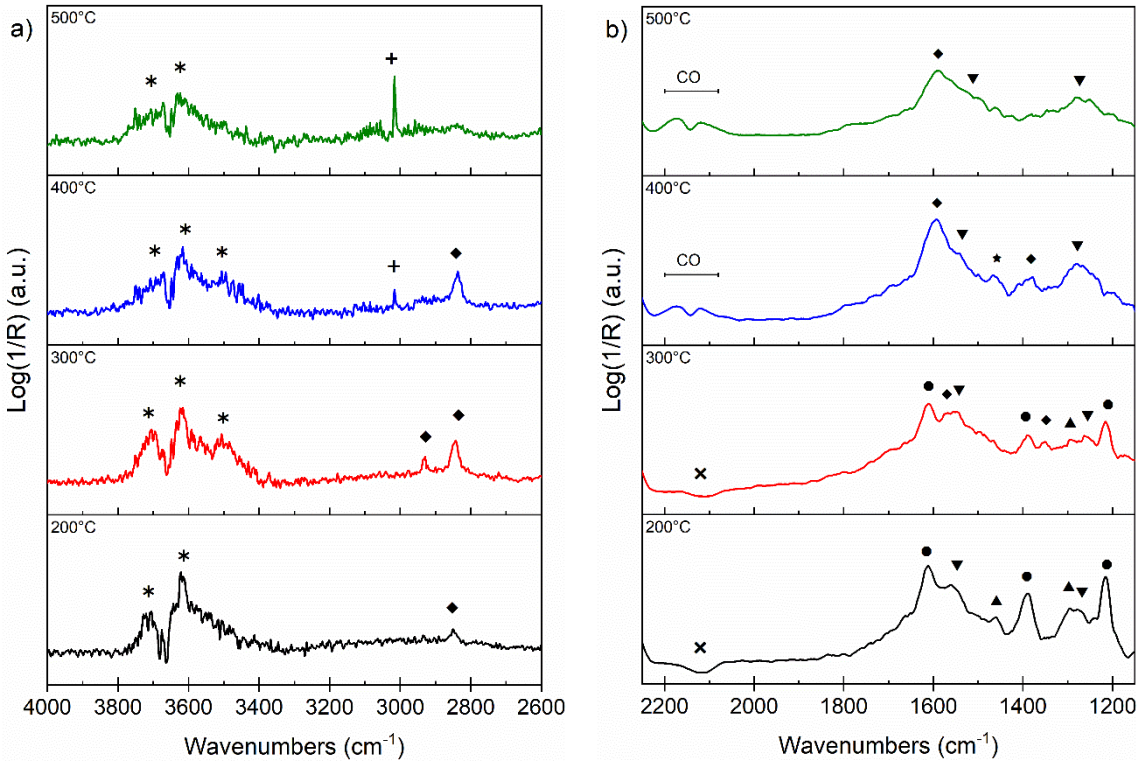

Figure 8. DRIFT spectra of nR support exposed to reaction mixture CO_2:H_2:He = 5:20:25 cm^3 min^{-1} from 200–500 °C between 4000–2600 cm^{-1} (**a**), and 2150 and 1150 cm^{-1} (**b**). Before the experiment, the sample was reduced in situ at 500 °C. Symbol definition: * hydroxide species, ◆ formate, + CH_4, × Ce^{3+} electronic transition, ● bidentate bicarbonate, ▼ bidentate carbonate, ▲ monodentate carbonate, ★ carboxylate.

The interaction of CO_2 in combination with H_2 over the CeO_2 surface was already evident at 200 °C by the appearance of a weak band at 2845 cm^{-1}, due to ν(CH) vibrations of formate species [52,53]. This band increased in intensity with a temperature up to 400 °C, and was accompanied by another less intense band at 2931 cm^{-1}, due to the corresponding $\nu_a(CO_2)$ + δ(CH) vibrations [52,53]. As the temperature continued to rise, the intensity of these bands decreased rapidly. Other bands appeared from 400 °C onwards due to the formation of methane (band at 3015 cm^{-1}) and carbon monoxide (see bands at 2117 and 2174 cm^{-1} in Figure 8b).

In the region between 2200 and 1150 cm^{-1}, the observed bands are mainly due to the interaction of CO_2 with the CeO_2 surface. It is important to emphasize that pre-reduction up to 500 °C guarantees a Ce^{3+} containing layers (surface-subsurface), as evidenced by a

negative, although not very intense, peak at 2114 cm^{-1} corresponding to the Ce^{3+} electronic transition, a phenomenon also observed on CeO_2 solid solutions with aliovalent elements, such as Gd^{3+} or Sm^{3+} by M. Grünbacher et al. [54]. At 200 °C, intense bands appeared at 1612, 1390, and 1216 cm^{-1} assigned to the $\nu_a(CO_3)$, $\nu_s(CO_3)$ and δ(OH) vibrations of bicarbonate species chemisorbed on reduced CeO_2 [12,52,55,56]. Numerous other bands have been discovered that are not yet clearly resolved, but we can focus on the most important ones: the bands at 1562 and 1272 cm^{-1} are due to the $\nu_a(CO_3)$ and $\nu_s(CO_3)$ vibrations of bidentate carbonate; whereas the bands at 1462 and 1293 cm^{-1} should come from the $\nu_a(CO_3)$ vibrations of monodentate carbonate [55–57].

In agreement with the spectra in Figure 8a, as the temperature increased, the vibrations associated with formate species became more intense, and the signal from the bands associated with bicarbonates (1612, 1390, and 1216 cm^{-1}) gradually decreased. The formate species, probably in a bidentate configuration, showed characteristic bands at 1569 and 1352 cm^{-1} due to the $\nu_a(CO_2)$ and $\nu_s(CO_2)$+ δ(CH) vibrations, respectively. These bands were most pronounced up to the highest temperature of 500 °C, but the interaction of CO_2 on the CeO_2 surface remained evident through other bands at ~1562 and ~1272 cm^{-1} associated with bidentate carbonate. In addition, a band at 1465 cm^{-1} was detected at 400 °C that could be due to the $\nu_a(CO_2)$ vibration of carboxylate [58,59]. This species was observed at the same temperature at which the CO bands were detected, so it was attributed to a possible reactive intermediate of its own formation. On the other hand, the CO bands can occur by the decomposition of the formate, or even by the CO_2 splitting as a result of a redox process involving the oxygen gap present on the reduced CeO_2 (CO_2 + Ce-□-Ce → CO + Ce-O-Ce) [20].

The introduction of Ni significantly changed the intermediate species detected by the DRIFT technique in the Ni-nR sample compared to the nR support. As can be seen in Figure 9a, the peaks characteristic of Ce-OH species, due to mono-coordinated (type I, 3710 cm^{-1}), bridged (type II, 3611 cm^{-1}) and triple-bridged (type III, 3541 cm^{-1}) hydroxyl bands, were very intense already at 200 °C, while especially the latter could only be detected in the support at the highest temperature; between 300–400 °C. As the temperature increased, the intensity of Ce-OH species decreased rapidly, and the band at 3641 cm^{-1} was no longer detected at 300 °C. From 400 °C, a significant increase in the absorption of the hydroxyl bands at lower wavenumbers indicated the presence of H-bonds due to the formation of H_2O [49]. The labile peak at 2847 cm^{-1}, associated with the ν(CH) vibration of formats, was already present at 200 °C, and increased significantly in intensity, up to 300 °C. At this temperature, the peak due to methane began to appear at 3016 cm^{-1}. With increasing temperatures, the ν(CH) oscillation of formates decreased abruptly and was barely detected from 400 °C, while the peak due to CH_4 was the most important up to the highest temperature of 500 °C.

As reported in Figure 9b, between 2200 and 1100 cm^{-1}, there were intense peaks around 1590 cm^{-1}, due to the $\nu_a(CO_2)$ oscillation of mono- and bidentate formates, with a shoulder at ~1541 cm^{-1} due to the $\nu_s(CO_3)$ of bidentate carbonates, and a broad peak at 1279 cm^{-1} corresponding to the $\nu_s(CO_3)$ of bidentate carbonate bands. Significantly, other carbonate species were undetectable, even at the lowest temperature of 200 °C, but were observed instead in the nR carrier. With increasing temperature, the presence of formates and bidentate carbonates on the surface persisted, but with a progressive decrease in intensity. In addition, a sharp band was observed at 1304 cm^{-1} from 400 °C onwards, corresponding to the ν_3(CH) vibrations of methane. At the highest temperature of 500 °C, the $\nu_a(CO_2)$ vibration due to carboxylates appeared at ~1462 cm^{-1}, together with faint peaks of CO, which, as in the case of the nR support, can be formed by the dissociation of CO_2 at this high temperature. In addition, it is essential to emphasize that no bands associated with Ni-$(CO)_x$ species were detected throughout the temperature range studied.

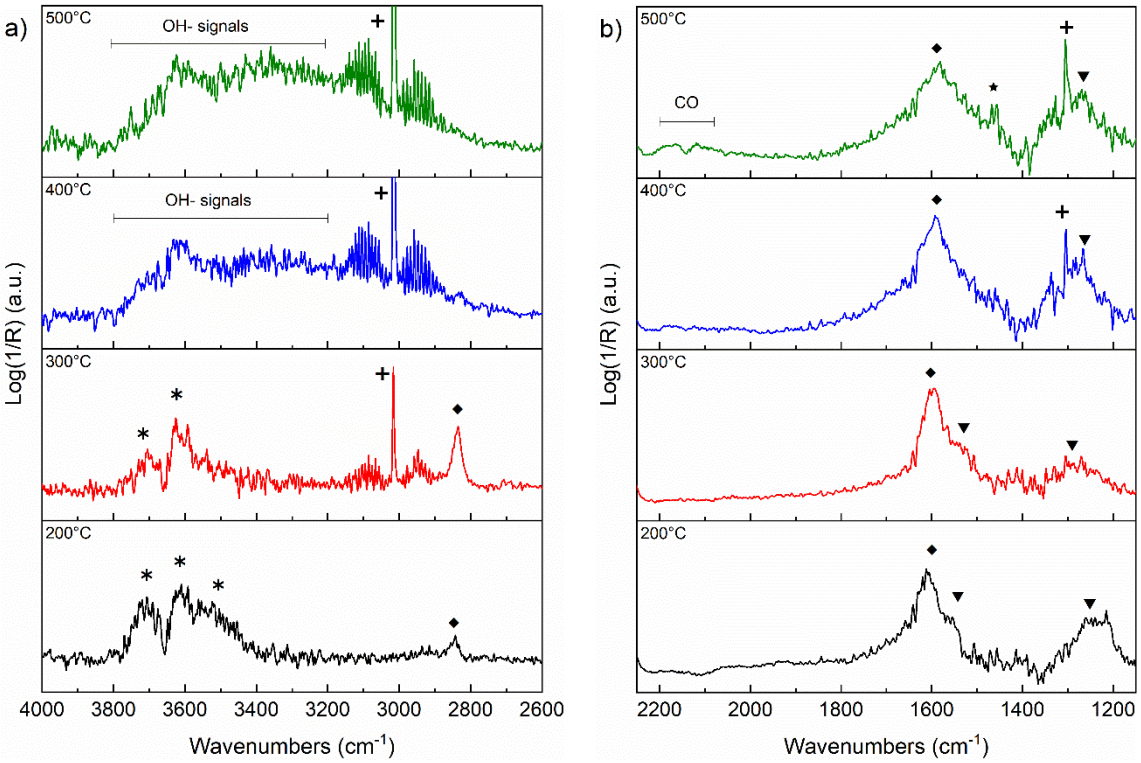

Figure 9. DRIFT spectra of Ni-nR catalyst exposed to reaction mixture CO_2:H_2:He = 5:20:25 cm^3 min^{-1} from 200–400 °C between 4000–2600 cm^{-1} (**a**), and 2150 and 1150 cm^{-1} (**b**). Before the experiment, the sample was reduced in situ at 500 °C. Symbol definition: * hydroxide species, ◆ formate, + CH_4, ▼ bidentate carbonate, ★ carboxylate.

From the chemical species that can act as the main reaction intermediates on the nR and Ni-nR systems, the following reaction steps during the CO_2 methanation can be hypothesized: (i) H_2 favors the formation of oxygen vacancies and Ce- OH species; (ii) CO_2 is chemisorbed on the "basic" $CeO_{2-\delta}$ surface forming carbonates (mainly bidentate); (iii) the conversion of carbonates to formates, is obtained at high temperatures on the $CeO_{2-\delta}$ support; (iv) Ni^0 plays a crucial role in the activation of the H_2 molecule through its dissociation into reactive H*, and thus its spillover on the CeO_δ surface; (v) the hydrogen spillover by Ni^0 favors the formation of formates at low temperature and their hydrogenation to CH_4.

To better clarify the methanation reaction pathway, we also performed an in operando DRIFT during CO hydrogenation. The characterization was carried out up to the maximum temperature of 400 °C. Figure 10a shows a magnification between 4000–2600 cm^{-1} and Figure 10b in the interval 2150 and 1150 cm^{-1}. At the temperature of 200 °C, very labile bands assigned to Ce-OH were observed, whereas monodentate formate was already evident with the ν(CH) and $\nu_a(CO_2)$ vibrations at 2831 and 1602 cm^{-1}, respectively. In addition to the bands associated with gaseous CO, there was an intense peak at 2059 cm^{-1} assigned to ν(CO-Ni) of linear nickel carbonyl and other unresolved bands between ~1960 and ~1680 cm^{-1}, probably due to bridged nickel carbonyl vibrations. Increasing the temperature to 300 °C favored a significant methane formation, with characteristic bands at 3016 and 1305 cm^{-1}. Moreover, the intensity of the formate bands, mainly the bidentate type at 2830 and 1596 cm^{-1}, increased alongside a significant decrease in the CO and Ni-CO bands. At the maximum temperature of 400 °C, there was a marked decrease in all formate bands, the absence of Ni-CO species, and the prominent bands were only those of CH_4 gas. In general, the presence of carbonates was not observed at any temperature. The CO was never oxidized by an oxygen storage process through the CeO_2, as no band of CO_2 was observed, clearly indicating that the surface was always maintained in a CeO_δ reduced state.

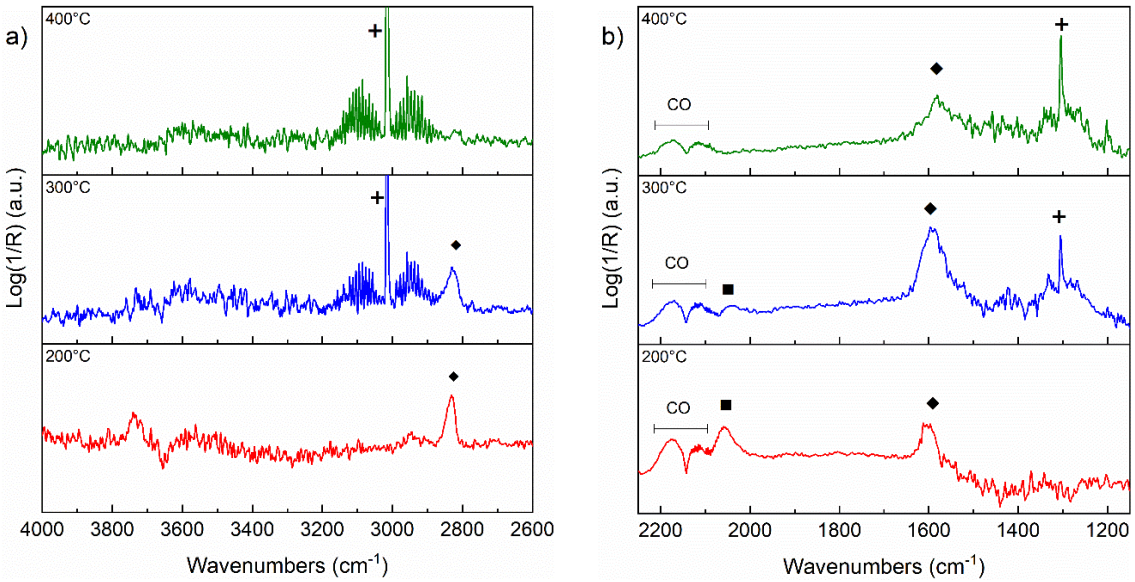

Figure 10. DRIFT spectra of Ni-nR catalyst exposed to reaction mixture CO:H_2:He = 5:15:30 cm^3 min^{-1} from 200–400 °C between 4000–2600 cm^{-1} (**a**), and 2150 and 1150 cm^{-1} (**b**). Before the experiment, the sample was reduced in situ at 500 °C. Symbol definition: ◆ formate, + CH_4, ■ linear CO on Ni.

It has been shown that the hydrogenation of CO can follow a mechanism involving formates [60]. In this case, they were also formed by exploiting the hydroxyl and the oxygen vacancy formed upon $Ce^{4+} \rightarrow Ce^{3+}$ reduction by H_2. Indeed, the low intensity of the Ce-OH species observed in Figure 10 could be a confirmation of this. The formates were then converted to CH_4 thanks to the spillover effect of H* generated by the dissociation of H_2 chemisorbed on the Ni^0 surface, as stated before. The CO chemisorbed on Ni could act as a spectator and not be directly hydrogenated to methane.

Thus, to summarize the results obtained with the DRIFT technique, it is possible to define Ni-nR as a bifunctional system, in which Ni plays a fundamental role in the activation of H_2, while $CeO_{2-\delta}$ acts on CO_2. Obviously, in our catalyst with a low Ni loading, the exposed surface is mainly that of CeO_δ. Therefore, the activation of CO_2 (carbonates, formates) is kept "constant" over a wide range of CO_2 partial pressure. This hypothesis is confirmed by the dependence of the reaction rate equation, exclusively on the partial pressure of H_2, as mentioned above, i.e., $-r_{CO_2} = k \cdot P_{H_2}^{0.68} \cdot P_{CO_2}^{0.06} \approx k \cdot P_{H_2}^{0.68}$.

4. Conclusions

$Ni_{0.05}Ce_{0.95}O_{2-\delta}$ catalysts, with nanorod and nanocube morphologies, were synthesized by hydrothermal methods. The most active catalyst for CO_2 methanation was the one with nanorod morphology, due to its strong metal–support interaction and its high reducibility, which favors the presence of oxygen vacancies. A high methane selectivity of about 90% was achieved over a wide temperature range up to 400 °C. No carbon residues were detected after the catalytic tests. The reaction rate essentially depended on the partial pressure of hydrogen. The DRIFT characterization showed that $CeO_{2-\delta}$ strongly interacted with the CO_2 molecule, adsorbed as various carbonates, while Ni^0 participated in the H_2 spillover. The absence of metal carbonyls and the considerable formation of chemisorbed formates on the $CeO_{2-\delta}$ support indicate a direct formate-type reaction mechanism. $Ni_{0.05}Ce_{0.95}O_{2-\delta}$ is thus a bifunctional system. At high temperatures (i.e., above 400 °C), CO can be formed by the dissociation of $CO_2 \rightarrow CO + 1/2O_2$, with a redox mechanism involving the oxygen vacancies of $CeO_{2-\delta}$. The presence of formate was also observed in the hydrogenation of CO, together with the formation of carbonyls absorbed on Ni. This finding suggests an important role of formate species also in the hydrogenation of CO.

Supplementary Materials: The following are available online at https://www.mdpi.com/article/10.3390/pr9111899/s1, Figure S1: Average size distribution: Ni-nR CeO_2 oxide width (a), Ni-nR CeO_2 oxide length (b), Ni-nR Ni oxide particles (c), oxide width of CeO_2 in the Ni-nC (d), Ni oxide particles in the Ni-nC (e).

Author Contributions: Conceptualization, I.L.; formal analysis, I.L., investigation, I.L., J.K.K., S.M.S.K., K.S.; resources, S.T.; data curation, I.L., J.K.K., U.P.L., S.T., S.S.; writing—original draft preparation, I.L.; writing—review and editing, S.T., S.S., U.P.L.; supervision, I.L.; project administration, G.I. All authors have read and agreed to the published version of the manuscript.

Funding: This research received no external funding.

Institutional Review Board Statement: Not applicable.

Informed Consent Statement: Not applicable.

Data Availability Statement: Not applicable.

Conflicts of Interest: The authors declare no conflict of interest.

References

1. Centi, G.; Perathoner, S. Opportunities and prospects in the chemical recycling of carbon dioxide to fuels. *Catalysis Today* **2009**, *148*, 191–205. [CrossRef]
2. Wang, W.; Wang, S.; Ma, X.; Gong, J. Recent advances in catalytic hydrogenation of carbon dioxide. *Chem. Soc. Rev.* **2011**, *40*, 3703–3727. [CrossRef]
3. Jomjaree, T.; Sintuya, P.; Srifa, A.; Koo-amornpattana, W.; Kiatphuengporn, S.; Assabumrungrat, S.; Sudoh, M.; Watanabe, R.; Fukuhara, C.; Ratchahat, S. Catalytic performance of Ni catalysts supported on CeO_2 with different morphologies for low-temperature CO_2 methanation. *Catal. Today* **2020**. [CrossRef]
4. Rönsch, S.; Schneider, J.; Matthischke, S.; Schlüter, M.; Götz, M.; Lefebvre, J.; Prabhakaran, P.; Bajohr, S. Review on methanation—From fundamentals to current projects. *Fuel* **2016**, *166*, 276–296. [CrossRef]
5. Hidalgo, D.; Martín-Marroquín, J.M. Power-to-methane, coupling CO_2 capture with fuel production: An overview. *Renew. Sustain. Energy Rev.* **2020**, *132*, 110057. [CrossRef]
6. Ashok, J.; Pati, S.; Hongmanorom, P.; Tianxi, Z.; Junmei, C.; Kawi, S. A review of recent catalyst advances in CO_2 methanation processes. *Catal. Today* **2020**, *356*, 471–489. [CrossRef]
7. Fan, W.K.; Tahir, M. Recent trends in developments of active metals and heterogenous materials for catalytic CO_2 hydrogenation to renewable methane: A review. *J. Environ. Chem. Eng.* **2021**, *9*, 105460. [CrossRef]
8. Lee, W.J.; Li, C.; Prajitno, H.; Yoo, J.; Patel, J.; Yang, Y.; Lim, S. Recent trend in thermal catalytic low temperature CO_2 methanation: A critical review. *Catal. Today* **2021**, *368*, 2–19. [CrossRef]
9. Aziz, M.A.A.; Jalil, A.A.; Triwahyono, S.; Ahmad, A. CO_2 methanation over heterogeneous catalysts: Recent progress and future prospects. *Green Chem.* **2015**, *17*, 2647–2663. [CrossRef]
10. Younas, M.; Loong Kong, L.; Bashir, M.J.K.; Nadeem, H.; Shehzad, A.; Sethupathi, S. Recent Advancements, Fundamental Challenges, and Opportunities in Catalytic Methanation of CO_2. *Energy Fuels* **2016**, *30*, 8815–8831. [CrossRef]
11. Li, W.; Wang, H.; Jiang, X.; Zhu, J.; Liu, Z.; Guo, X.; Song, C. A short review of recent advances in CO_2 hydrogenation to hydrocarbons over heterogeneous catalysts. *RSC Adv.* **2018**, *8*, 7651–7669. [CrossRef]
12. Lee, S.M.; Lee, Y.H.; Moon, D.H.; Ahn, J.Y.; Nguyen, D.D.; Chang, S.W.; Kim, S.S. Reaction Mechanism and Catalytic Impact of Ni/CeO_{2-x} Catalyst for Low-Temperature CO_2 Methanation. *Ind. Eng. Chem. Res.* **2019**, *58*, 8656–8662. [CrossRef]
13. Shen, L.; Xu, J.; Zhu, M.; Han, Y.-F. Essential Role of the Support for Nickel-Based CO_2 Methanation Catalysts. *ACS Catal.* **2020**, *10*, 14581–14591. [CrossRef]
14. Lin, L.; Gerlak, C.A.; Liu, C.; Llorca, J.; Yao, S.; Rui, N.; Zhang, F.; Liu, Z.; Zhang, S.; Deng, K.; et al. Effect of Ni particle size on the production of renewable methane from CO_2 over Ni/CeO_2 catalyst. *J. Energy Chem.* **2021**, *61*, 602–611. [CrossRef]
15. Wang, L.; Deo, S.; Dooley, K.; Janik, M.J.; Rioux, R.M. Influence of metal nuclearity and physicochemical properties of ceria on the oxidation of carbon monoxide. *Chin. J. Catal.* **2020**, *41*, 951–962. [CrossRef]
16. Moeini, S.S.; Battocchio, C.; Casciardi, S.; Luisetto, I.; Lupattelli, P.; Tofani, D.; Tuti, S. Oxidized Palladium Supported on Ceria Nanorods for Catalytic Aerobic Oxidation of Benzyl Alcohol to Benzaldehyde in Protic Solvents. *Catalysts* **2019**, *9*, 847. [CrossRef]
17. Lei, Y.; Li, W.; Liu, Q.; Lin, Q.; Zheng, X.; Huang, Q.; Guan, S.; Wang, X.; Wang, C.; Li, F. Typical crystal face effects of different morphology ceria on the activity of Pd/CeO_2 catalysts for lean methane combustion. *Fuel* **2018**, *233*, 10–20. [CrossRef]
18. Luisetto, I.; Tuti, S.; Di Bartolomeo, E. Co and Ni supported on CeO_2 as selective bimetallic catalyst for dry reforming of methane. *Int. J. Hydrogen Energy* **2012**, *37*, 15992–15999. [CrossRef]
19. Luisetto, I.; Tuti, S.; Battocchio, C.; Lo Mastro, S.; Sodo, A. $Ni/CeO_2–Al_2O_3$ catalysts for the dry reforming of methane: The effect of $CeAlO_3$ content and nickel crystallite size on catalytic activity and coke resistance. *Appl. Catal. A Gen.* **2015**, *500*, 12–22. [CrossRef]

20. Luisetto, I.; Tuti, S.; Romano, C.; Boaro, M.; Di Bartolomeo, E.; Kesavan, J.K.; Kumar, S.S.; Selvakumar, K. Dry reforming of methane over Ni supported on doped CeO_2: New insight on the role of dopants for CO_2 activation. *J. CO_2 Util.* **2019**, *30*, 63–78. [CrossRef]
21. Gao, X.; Zhu, S.; Dong, M.; Wang, J.; Fan, W. Ru/CeO_2 catalyst with optimized CeO_2 morphology and surface facet for efficient hydrogenation of ethyl levulinate to γ-valerolactone. *J. Catal.* **2020**, *389*, 60–70. [CrossRef]
22. Marconi, E.; Tuti, S.; Luisetto, I. Structure-Sensitivity of CO_2 Methanation over Nanostructured Ni Supported on CeO_2 Nanorods. *Catalysts* **2019**, *9*, 375. [CrossRef]
23. Iglesias, I.; Quindimil, A.; Mariño, F.; De-La-Torre, U.; González-Velasco, J.R. Zr promotion effect in CO_2 methanation over ceria supported nickel catalysts. *Int. J. Hydrogen Energy* **2019**, *44*, 1710–1719. [CrossRef]
24. Ocampo, F.; Louis, B.; Roger, A.-C. Methanation of carbon dioxide over nickel-based $Ce_{0.72}Zr_{0.28}O_2$ mixed oxide catalysts prepared by sol–gel method. *Appl. Catal. A Gen.* **2009**, *369*, 90–96. [CrossRef]
25. Sakpal, T.; Lefferts, L. Structure-dependent activity of CeO_2 supported Ru catalysts for CO_2 methanation. *J. Catal.* **2018**, *367*, 171–180. [CrossRef]
26. Ren, Z.; Peng, F.; Li, J.; Liang, X.; Chen, B. Morphology-Dependent Properties of Cu/CeO_2 Catalysts for the Water-Gas Shift Reaction. *Catalysts* **2017**, *7*, 48. [CrossRef]
27. Du, X.; Zhang, D.; Shi, L.; Gao, R.; Zhang, J. Morphology Dependence of Catalytic Properties of Ni/CeO_2 Nanostructures for Carbon Dioxide Reforming of Methane. *J. Phys. Chem. C* **2012**, *116*, 10009–10016. [CrossRef]
28. Wang, S.; Zhao, L.; Wang, W.; Zhao, Y.; Zhang, G.; Ma, X.; Gong, J. Morphology control of ceria nanocrystals for catalytic conversion of CO_2 with methanol. *Nanoscale* **2013**, *5*, 5582–5588. [CrossRef]
29. Trovarelli, A.; Llorca, J. Ceria Catalysts at Nanoscale: How Do Crystal Shapes Shape Catalysis? *ACS Catal.* **2017**, *7*, 4716–4735. [CrossRef]
30. Ye, R.-P.; Li, Q.; Gong, W.; Wang, T.; Razink, J.J.; Lin, L.; Qin, Y.-Y.; Zhou, Z.; Adidharma, H.; Tang, J.; et al. High-performance of nanostructured Ni/CeO_2 catalyst on CO_2 methanation. *Appl. Catal. B Environ.* **2020**, *268*, 118474. [CrossRef]
31. Padi, S.P.; Shelly, L.; Komarala, E.P.; Schweke, D.; Hayun, S.; Rosen, B.A. Coke-free methane dry reforming over nano-sized NiO-CeO_2 solid solution after exsolution. *Catal. Commun.* **2020**, *138*, 105951. [CrossRef]
32. Thommes, M.; Kaneko, K.; Neimark, A.V.; Olivier, J.P.; Rodriguez-Reinoso, F.; Rouquerol, J.; Sing, K.S.W. Physisorption of gases, with special reference to the evaluation of surface area and pore size distribution (IUPAC Technical Report). *Pure Appl. Chem.* **2015**, *87*, 1051–1069. [CrossRef]
33. Perrichon, V.; Laachir, A.; Bergeret, G.; Fréty, R.; Tournayan, L.; Touret, O. Reduction of cerias with different textures by hydrogen and their reoxidation by oxygen. *J. Chem. Soc. Faraday Trans.* **1994**, *90*, 773–781. [CrossRef]
34. Désaunay, T.; Bonura, G.; Chiodo, V.; Freni, S.; Couzinié, J.P.; Bourgon, J.; Ringuedé, A.; Labat, F.; Adamo, C.; Cassir, M. Surface-dependent oxidation of H_2 on CeO_2 surfaces. *J. Catal.* **2013**, *297*, 193–201. [CrossRef]
35. Giordano, F.; Trovarelli, A.; de Leitenburg, C.; Giona, M. A Model for the Temperature-Programmed Reduction of Low and High Surface Area Ceria. *J. Catal.* **2000**, *193*, 273–282. [CrossRef]
36. Xiao, Z.; Li, Y.; Hou, F.; Wu, C.; Pan, L.; Zou, J.; Wang, L.; Zhang, X.; Liu, G.; Li, G. Engineering oxygen vacancies and nickel dispersion on CeO2 by Pr doping for highly stable ethanol steam reforming. *Appl. Catal. B Environ.* **2019**, *258*, 117940. [CrossRef]
37. Takeguchi, T.; Furukawa, S.-n.; Inoue, M. Hydrogen Spillover from NiO to the Large Surface Area CeO_2–ZrO_2 Solid Solutions and Activity of the NiO/CeO_2–ZrO_2 Catalysts for Partial Oxidation of Methane. *J. Catal.* **2001**, *202*, 14–24. [CrossRef]
38. Varvoutis, G.; Lykaki, M.; Stefa, S.; Papista, E.; Carabineiro, S.A.C.; Marnellos, G.E.; Konsolakis, M. Remarkable efficiency of Ni supported on hydrothermally synthesized CeO_2 nanorods for low-temperature CO_2 hydrogenation to methane. *Catal. Commun.* **2020**, *142*, 106036. [CrossRef]
39. Safa, S.; Hejazi, R.; Rabbani, M.; Azimirad, R. Hydrothermal synthesis of NiO nanostructures for photodegradation of 4-nitrophenol. *Desalin. Water Treat.* **2016**, *57*, 21982–21989. [CrossRef]
40. Kumar, J.P.; Giri, S.D.; Sarkar, A. Mesoporous NiO with different morphology: Synthesis, characterization and their evaluation for oxygen evolution reaction. *Int. J. Hydrogen Energy* **2018**, *43*, 15639–15649. [CrossRef]
41. Torrente-Murciano, L.; Gilbank, A.; Puertolas, B.; Garcia, T.; Solsona, B.; Chadwick, D. Shape-dependency activity of nanostructured CeO2 in the total oxidation of polycyclic aromatic hydrocarbons. *Appl. Catal. B Environ.* **2013**, *132-133*, 116–122. [CrossRef]
42. Wang, N.; Qian, W.; Chu, W.; Wei, F. Crystal-plane effect of nanoscale CeO_2 on the catalytic performance of Ni/CeO_2 catalysts for methane dry reforming. *Catal. Sci. Technol.* **2016**, *6*, 3594–3605. [CrossRef]
43. Wu, H.C.; Chang, Y.C.; Wu, J.H.; Lin, J.H.; Lin, I.K.; Chen, C.S. Methanation of CO_2 and reverse water gas shift reactions on Ni/SiO_2 catalysts: The influence of particle size on selectivity and reaction pathway. *Catal. Sci. Technol.* **2015**, *5*, 4154–4163. [CrossRef]
44. Kesavan, J.K.; Luisetto, I.; Tuti, S.; Meneghini, C.; Iucci, G.; Battocchio, C.; Mobilio, S.; Casciardi, S.; Sisto, R. Nickel supported on YSZ: The effect of Ni particle size on the catalytic activity for CO_2 methanation. *J. CO_2 Util.* **2018**, *23*, 200–211. [CrossRef]
45. Gao, J.; Wang, Y.; Ping, Y.; Hu, D.; Xu, G.; Gu, F.; Su, F. A thermodynamic analysis of methanation reactions of carbon oxides for the production of synthetic natural gas. *RSC Adv.* **2012**, *2*, 2358–2368. [CrossRef]

46. Laachir, A.; Perrichon, V.; Badri, A.; Lamotte, J.; Catherine, E.; Lavalley, J.C.; El Fallah, J.; Hilaire, L.; Le Normand, F.; Quéméré, E.; et al. Reduction of CeO_2 by hydrogen. Magnetic susceptibility and Fourier-transform infrared, ultraviolet and X-ray photoelectron spectroscopy measurements. *J. Chem. Soc. Faraday Trans.* **1991**, *87*, 1601–1609. [CrossRef]
47. Binet, C.; Daturi, M.; Lavalley, J.-C. IR study of polycrystalline ceria properties in oxidised and reduced states. *Catal. Today* **1999**, *50*, 207–225. [CrossRef]
48. López, J.M.; Gilbank, A.L.; García, T.; Solsona, B.; Agouram, S.; Torrente-Murciano, L. The prevalence of surface oxygen vacancies over the mobility of bulk oxygen in nanostructured ceria for the total toluene oxidation. *Appl. Catal. B Environ.* **2015**, *174-175*, 403–412. [CrossRef]
49. Luo, L.; LaCoste, J.D.; Khamidullina, N.G.; Fox, E.; Gang, D.D.; Hernandez, R.; Yan, H. Investigate interactions of water with mesoporous ceria using in situ VT-DRIFTS. *Surf. Sci.* **2020**, *691*, 121486. [CrossRef]
50. Proaño, L.; Tello, E.; Arellano-Trevino, M.A.; Wang, S.; Farrauto, R.J.; Cobo, M. In-situ DRIFTS study of two-step CO_2 capture and catalytic methanation over Ru,"Na_2O"/Al_2O_3 Dual Functional Material. *Appl. Surf. Sci.* **2019**, *479*, 25–30. [CrossRef]
51. Cárdenas-Arenas, A.; Quindimil, A.; Davó-Quiñonero, A.; Bailón-García, E.; Lozano-Castelló, D.; De-La-Torre, U.; Pereda-Ayo, B.; González-Marcos, J.A.; González-Velasco, J.R.; Bueno-López, A. Isotopic and in situ DRIFTS study of the CO_2 methanation mechanism using Ni/CeO_2 and Ni/Al_2O_3 catalysts. *Appl. Catal. B Environ.* **2020**, *265*, 118538. [CrossRef]
52. Tada, S.; Nagase, H.; Fujiwara, N.; Kikuchi, R. What Are the Best Active Sites for CO_2 Methanation over Ni/CeO_2? *Energy Fuels* **2021**, *35*, 5241–5251. [CrossRef]
53. Köck, E.-M.; Kogler, M.; Bielz, T.; Klötzer, B.; Penner, S. In Situ FT-IR Spectroscopic Study of CO_2 and CO Adsorption on Y_2O_3, ZrO_2, and Yttria-Stabilized ZrO_2. *J. Phys. Chem. C* **2013**, *117*, 17666–17673. [CrossRef] [PubMed]
54. Grünbacher, M.; Klötzer, B.; Penner, S. CO_2 Reduction by Hydrogen Pre-Reduced Acceptor-Doped Ceria. *ChemPhysChem* **2019**, *20*, 1706–1718. [CrossRef]
55. Jia, X.; Zhang, X.; Rui, N.; Hu, X.; Liu, C.-j. Structural effect of Ni/ZrO_2 catalyst on CO_2 methanation with enhanced activity. *Appl. Catal. B Environ.* **2019**, *244*, 159–169. [CrossRef]
56. Solis-Garcia, A.; Louvier-Hernandez, J.F.; Almendarez-Camarillo, A.; Fierro-Gonzalez, J.C. Participation of surface bicarbonate, formate and methoxy species in the carbon dioxide methanation catalyzed by ZrO_2-supported Ni. *Appl. Catal. B Environ.* **2017**, *218*, 611–620. [CrossRef]
57. Tada, S.; Ochieng, O.J.; Kikuchi, R.; Haneda, T.; Kameyama, H. Promotion of CO_2 methanation activity and CH_4 selectivity at low temperatures over Ru/CeO_2/Al_2O_3 catalysts. *Int. J. Hydrogen Energy* **2014**, *39*, 10090–10100. [CrossRef]
58. Jin, T.; Zhou, Y.; Mains, G.J.; White, J.M. Infrared and x-ray photoelectron spectroscopy study of carbon monoxide and carbon dioxide on platinum/ceria. *J. Phys. Chem.* **1987**, *91*, 5931–5937. [CrossRef]
59. Shido, T.; Iwasawa, Y. Regulation of reaction intermediate by reactant in the water-gas shift reaction on CeO_2, in relation to reactant-promoted mechanism. *J. Catal.* **1992**, *136*, 493–503. [CrossRef]
60. Li, C.; Sakata, Y.; Arai, T.; Domen, K.; Maruya, K.-I.; Onishi, T. Adsorption of carbon monoxide and carbon dioxide on cerium oxide studied by Fourier-transform infrared spectroscopy. Part 2.—Formation of formate species on partially reduced CeO_2 at room temperature. *J. Chem. Soc. Faraday Trans. 1 Phys. Chem. Condens. Ph.* **1989**, *85*, 1451–1461. [CrossRef]